

Time-Resolved Penetration of B₄C Tiles by the APM2 Bullet

Charles E. Anderson, Jr.¹, Matthew S. Burkins², James D. Walker¹, and William A. Gooch²

Abstract: A modification of Wilkins computational ceramics model is used to simulate experiments of the impact of the APM2 bullet against boron carbide/aluminum targets. Flash radiography provides time-resolved penetration histories. The simulation results are compared to the experimental data; generally, agreement is very good, including capturing dwell and then the onset of penetration. Crater width and debris diameter are also reproduced by the simulations reasonably well. A critical discussion of deficiencies of this computational engineering model is provided.

keyword: ceramic modeling, dwell, boron carbide, APM2 bullet, ceramic tile, numerical simulations, constitutive modeling, time-resolved data

1 Introduction

The classic study of Wilkins and coworkers in 1967-1969 [Wilkins (1968), Wilkins (1978)] provided the first high speed photographic images and X-ray shadowgraphs (3 channels of 600 KeV) of small arms projectiles impacting ceramic targets. Wilkins used a monolithic hard steel (R_c55) projectile as a surrogate projectile for the 7.62-mm armor-piercing (AP) bullet. Wilkins also developed a phenomenological computational ceramics model for thin tiles and compared the results of numerical simulations—using the Lagrangian hydrocode HEMP [Wilkins (1981)]—with experiments. He then performed numerical parametric studies to investigate the influence of ceramic material properties on ballistic performance [Wilkins (1968), Wilkins (1978)].

The 7.62-mm APM2 bullet is exceedingly more complex than the monolithic surrogate used by Wilkins. A schematic of the bullet is shown in Fig. 1. The bullet consists of a jacket made of gilding metal (90% Cu, 10%

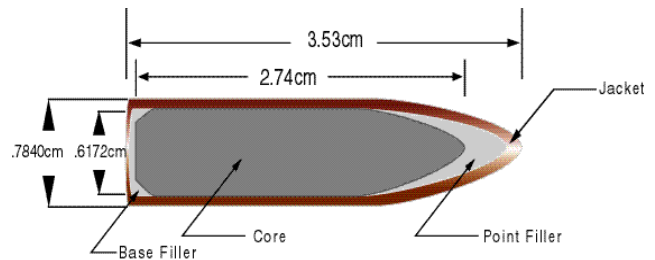


Figure 1 : Schematic of 7.62-mm APM2 bullet.

Zn), 4.21 g; a lead (Pb) nose element, 0.78 g; a Pb base filler, 0.50 g; and a very hard steel core, 5.25 g. The lead nose is pressed over the steel core and both are encased in the metal jacket. The masses are nominal values. Some lots of bullets do not contain the Pb base filler, and the Pb point filler is slightly more massive (1.3 g), with the total mass of the bullet still 10.6-10.7 g. The core design dates from 1939. The 1070 tool steel core has a classical ogive nose and boat tail design; the core is very hard, measuring Rockwell C62-65.

The U. S. Army Research Laboratory (ARL) adapted dual 1-MeV X-ray pulsers to obtain two shadowgraph images of the impact of the APM2 bullet impacting boron carbide (B₄C) [Gooch, Burkins, Kingman, Hauver, Netherwood, and Benck (1999), Gooch, Burkins, Hauver, Netherwood, and Benck (2000)]. Three conditions of the projectile were tested: the full metal jacket (FMJ) projectile; the lead (Pb) tip and steel core only; and just the steel core. The FMJ was removed by machining for tests with the core, or nose and core only. These conditions allowed the separation of the ballistic contributions of the projectile components. Numerical simulations using the Johnson-Holmquist ceramics constitutive model [Johnson and Holmquist (1999)] for B₄C were not in good agreement with the experiments [Gooch, Burkins, Kingman, Hauver, Netherwood, and Benck (1999)]. The authors report that the most obvious discrepancy was the inability of the simulations to

¹ Southwest Research Institute, P. O. Drawer 28510, San Antonio, Texas 78228 USA

² Army Research Laboratory, Aberdeen Proving Ground, MD 21005

replicate the erosion of the steel core [Gooch, Burkins, Kingman, Hauver, Netherwood, and Benck (1999)]. The fundamental cause for this failure to reproduce the experimental results is a consequence of the inability of the ceramics constitutive model to capture the phenomenon called *dwell*, where the impacting projectile flows radially at the ceramic front face and does not penetrate the ceramic. During dwell, the projectile loses kinetic energy due to mass loss and deceleration.

Walker, *et al* [Walker, Anderson, Jr., and Cox (1995a) and (1995b)] took Wilkins' computational ceramics model and implemented the model into CTH [McGlaun, Thompson, and Elrick (1990)]. The model was applied to Al₂O₃ ceramic tiles and the M80 ball round. Later, the model was applied to B₄C ceramic tiles impacted by Wilkins surrogate AP bullet, and modifications were required in order for the simulations to match experiment [Anderson, Jr. and Walker (2000)]. This modified model was used to simulate the reverse ballistic experiments for the three projectiles [Anderson, Jr. and Gooch (2001)]. Agreement was good, but with some qualifications concerning interpretation of the experiments.

Therefore, to eliminate the experimental uncertainties in the previous set of experiments, a second set of experiments was conducted; these experiments were performed in the conventional "forward ballistics" mode where the bullet is fired at a stationary target. This geometry eliminates any positional uncertainty in the target. A brief description of the experiments will be given, followed by a summary of the modifications made to the Wilkins ceramic model. Then the simulation results will be compared to the experimental data.

2 Experimental setup

Experiments were conducted on targets consisting of 7.62 mm of B₄C bonded to a 6.6-mm-thick 6061-T6 aluminum substrate. A 1-MeV flash X-ray system was used to obtain time-resolved images of penetration. One flash shadowgraph was obtained for each test. A schematic of the target is shown in Fig. 2. A lead tape (12.7-mm wide and approximately 1.6-mm thick) was placed between the ceramic and substrate, and positioned in the center of the target (below the impact point). The lead tape provided excellent definition of the position of the ceramic/substrate interface in the flash radiographs. A total of ten experiments were conducted; the delay time for the flash X-ray pulse was varied to provide position-

time data. The average impact velocity of the experiments was 834 m/s, with a variation of approximately ± 15 m/s. Measurements of the nose, tail, and ceramic interface positions, along with the position of the back surface of the aluminum plate, were made from the flash radiographs.

The X-ray times, based on the specifications of the electronic equipment, are accurate to ± 100 nanoseconds. The maximum accuracy of the position measurements is ± 0.25 mm; however, as these measurements are performed manually, a ± 0.5 -mm accuracy is probably more reasonable.

3 Numerical simulations

A variety of numerical techniques can be used to simulate this impact problem. Traditional Lagrangian formulations cannot handle the large distortions, but the use of eroding elements [Stecher and Johnson (1984)] permit calculations of impact problems. However, Johnson and Holmquist have found that eroding elements introduce pressure relaxation at the projectile-target interface, which is highly detrimental to accurate simulations of pressure-dependent constitutive behavior [Johnson, Beissel, and Holmquist (2002)]. Generalized particles [Johnson, Beissel, and Stryk (2000)] or meshless methods [Bardenhagen and Kober (2004), Atluri, Han, and Rajendran (2004)] are more appropriate for such impact calculations. Johnson and Holmquist have shown good reproduction of experiments using an algorithm that changes a finite element to a generalized particle [Johnson, Stryk, Beissel, and Holmquist (2002), Holmquist and Johnson (2002)]. Alternatively, an Eulerian formulation permits large distortions, and the incorporation of second-order advection [Predebon, Anderson, Jr., and Walker (1991)] and interface reconstruction algorithms have permitted Eulerian codes to reproduce quite accurately a wide range of penetration problems [Anderson, Jr. (2003)]. In this study, we have selected the Eulerian wavecode CTH [McGlaun, Thompson, and Elrick (1990)] for the computational study.

3.1 Modified Wilkins' ceramic constitutive model

As already mentioned, Anderson and Walker incorporated Wilkins' ceramic model into the Eulerian wavecode CTH and compared the computational results to flash X-ray shadowgraphs taken by Wilkins, *et al.* [Wilkins,

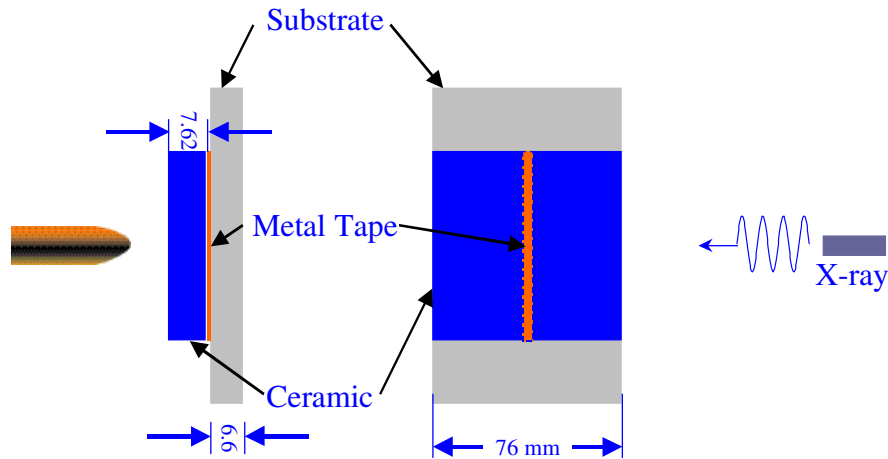


Figure 2 : Schematic of modified-target flash-radiography experiments.

Landingham, and Honodel (1970)] of a monolithic, hard steel (R_c55) steel projectile impacting B_4C tiles bonded to an aluminum substrate [Anderson, Jr. and Walker (2000)]. The simulation results did not agree with the results inferred from the X-ray images. Additionally, results from numerical simulations using the Wilkins model did not agree with experimental data for the APM2 bullet [Anderson, Jr. (1999)], specifically, the length of the core after perforating a ceramic target. To understand the discrepancies necessitated a re-examination of the model [Anderson, Jr. and Walker (2000)]. Two very important modifications were required for the computational model to replicate experimental observations. First, it was found that a description of the shear strength of the failed ceramic material is necessary. A Drucker-Prager model was incorporated into the overall ceramics model to account for the strength of failed ceramic.

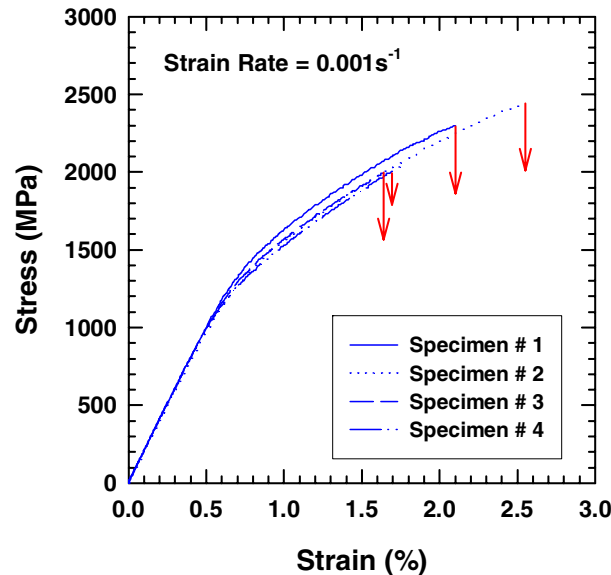
The second modification is associated with the speed of damage. The original model assumed that the transition of strength from intact to failed ceramic was associated with crack propagation. It was found that damage propagation had to be slowed significantly—by approximately a factor of 20 relative to a crack propagation velocity—for the simulations to replicate experimental details. Within the context of the model, a damage variable controls the maximum speed of damage propagation. It appears that there are two distinct phenomena concerning the impact and penetration of a ceramic tile. First, there is the appearance of cracks. Radial cracks appear first, the result of hoop tensile stresses, followed by circumferential cracks, forming fracture conoids. Al-

though these cracks certainly degrade the structural integrity of the ceramic, large pieces of ceramic remain in the path of the projectile. To penetrate, the projectile must “grind up” the ceramic—called comminution—into a very fine ceramic “powder.” This comminuted material is referred to as the Mescall zone [Shockey, Marchand, Skaggs, Cort, Burkett, and Parker (1990)]. It is this comminution process that dominates the penetration dynamics of ceramic tiles. With these modifications, simulations reproduce the ballistic limit experiments of Wilkins for boron carbide on an aluminum substrate [Anderson, Jr. and Walker (2000)].

The computational ceramics model, and the equations implemented, is summarized in the Appendix, including the modifications described above. The constants required for the model are: the intact strength Y_o , the tensile fracture stress σ_f , the slope of the Drucker-Prager curve b , the cap Y_{cap} , the shear modulus G , and the density ρ . (Since the bulk modulus κ is specified for the equation of state, Poisson’s ratio can be specified in lieu of G .) The material constants for boron carbide (B_4C) were obtained from Cercom [Palika (1999)] and from Johnson and Holmquist (1999). The material constants are: $Y_o = 12.1$ GPa; $\sigma_f = 0.3$ GPa; $b = 1.7$; $Y_{cap} = 4.0$ GPa; $\rho = 2.54$ g/cm³; $\kappa = 233$ GPa, and $\nu = 0.17$. The constant f_1 must be specified; it is the parameter that controls the speed of damage within a computational cell once fracture is initiated (see the Appendix). A value of 0.025 was used. The model permits initiation of failure in the hoop direction or only in the plane of motion. For the simulations reported here, failure initiation was constrained to

Table 1 : Constitutive Model Parameters

Material	ρ_o g/cm ³	C_o km/s	ν -	A (MPa)	β -	C -	n -	m -	T_{melt} K	c_p J/kg-K	Eqn. No.
Steel Core	7.80	4.5	0.29	1034	17.5	0.005	0.64	1.0	1790	478	1
Gilding Metal	8.94	3.94	0.35	500	0.0	0.025	1.0	1.0	1360	383	1
Lead	11.34	2.05	0.44	27.6	110	0.116	0.52	0.00116	760	124	2

**Figure 3** : Stress-strain curve for steel core.

be in the plane of motion.

All simulations described below used the cylindrical symmetric option of CTH [McGlaun, Thompson, and Elrick (1990)]. Twenty zones, with an aspect ratio of one, were used to resolve the radius of the projectile. The aspect ratio of one was maintained throughout the interaction region, but the radial zone size was allowed to grow (at approximately a 3% rate) approximately 8 mm from the axis of symmetry to the edge of the computational domain.

3.2 Constitutive Properties for Core and Jacket Materials

To model the APM2 bullet, the constitutive parameters of the materials in the bullet must be estimated. Stress-strain measurements were performed on the bullet core material. The stress-strain specimens were fabricated from bullet cores. Four specimens were tested; the test

results are shown in Fig. 3. The strain at failure varied from approximately 1.6% to 2.6%. Somewhat a surprise, even though the core material is extremely hard, the core material has a large strain hardening coefficient. Initial yield is approximately 1.2 GPa, and it hardens to approximately 2.0 – 2.5 GPa, depending upon when the material fails.

Likewise, the stress-strain behavior of the jacket (gilding metal) material was characterized. A challenge was making the specimens to conduct the stress-strain measurements since the specimens had to be fabricated from the actual jacket material. Slits were cut into the jacket, and the core removed. A fixture was designed to load the jacket ligaments in tension; strain gages were attached to the ligaments. Three specimens were tested, and the results are shown in Fig. 4. The gilding metal is quite strong, with a flow stress of approximately 500 MPa, which is about twice the flow stress of 6061-T6

aluminum.

Using these data, combined with experience of the constitutive response of metal alloys, Johnson [Johnson (1999)] estimated the constants for the Johnson-Cook constitutive model [Johnson and Cook (1983)]. These constants, along for those used for the Pb (which used the Steinberg-Guinan [Steinberg (1996)] model), are given in Table 1. Equations (1) and (2) are the Johnson-Cook and the Steinberg-Guinan equations, respectively. The entries in the table are the density ρ , bulk sound speed C_o ; Poisson's ratio ν ; constitutive constants A , β , C , n , and m ; melt temperature T_{melt} , and specific heat c_p . T^* is the homologous temperature.

$$\begin{aligned}\sigma_{eq} &= A (1 + \beta \epsilon_p^n) (1 + C \ln \dot{\epsilon}^*) (1 - T^{*m}) \\ \dot{\epsilon}^* &= \dot{\epsilon} / \dot{\epsilon}_0 \\ \dot{\epsilon}_0 &= 1.0 \text{s}^{-1} \\ T^* &= \frac{T_{melt} - T}{T_{melt} - T_{ref}} \\ T_{ref} &= 300 \text{ K}\end{aligned}\quad (1)$$

$$\begin{aligned}\sigma_{eq} &= A (1 + \beta \epsilon_p^n) \\ &\quad \left\{ 1 + C^* P \eta^{1/3} - m^* (T - 300) \right\} \\ \eta &= 1 - \frac{\rho_o}{\rho} \\ C^* &= C / (1.0 \text{ GPa}) \\ m^* &= m / (1.0 \text{ K})\end{aligned}\quad (2)$$

For implementation into CTH, a failure strain of 10% for the core material was used. This strain-to-failure value was used, in contrast to the measured 1.6% - 2.6%, because the core material is under compression during penetration, thereby allowing for larger strains than can be realized in tension.

3.3 Simulation of Experiments

The flash radiographs from the experiments are shown in Fig. 5, and some of the pertinent measurements are given in Table 2. There are several interesting observations. Dwell persists until approximately 18 μs . Conoid cracks can be seen in the original X-rays; these cracks appear to emanate from the projectile nose towards the substrate. In Fig. 5(d), it appears that erosion products from the projectile are perhaps "sliding" into one of these conoid regions. The projectile nose is not as deep in Fig. 5(e) as in 5(d), but it is clear that penetration of failed ceramic

has started. The erosion products from the projectile are relatively "flat" at the penetration front, and are spread over an area approximately 3.5 projectile diameters (i.e., ~ 12 times the projectile area).

The lead tape, readily visible in the original X-ray shadowgraphs, clearly helps to delineate the ceramic-substrate interface. An enlarged picture of Fig. 5(i) is shown in Fig. 6, and the position of the lead tape is denoted in the figure. The ceramic-substrate interface has moved a distance approximately equal to one-half the thickness of the substrate at the time of this flash X-ray picture. The position of the ceramic-substrate interface would have been misinterpreted if we had not had the lead tape (the displacements of the interface, underneath the projectile, would have been considerably underestimated).

A numerical simulation of the experiment was performed. The impact velocity for the simulation was 834 m/s. This represents an average of the impact velocities in the experiments. The velocities of the nose (penetration velocity), core tip, core tail, and tail of the bullet as a function of time are shown in Fig. 7. The vertical, dashed lines in the figure are the times of the flash X-rays (Table 2). The core tip impacts the ceramic surface at approximately 8 to 9 μs after initial impact ($t=0$). This results in a "spike" in the penetration velocity, but the penetration velocity returns to a relatively low value (~ 100 m/s). Dwell, or dwell-like behavior, persists until approximately 18-21 μs . Between 21 μs and 23 μs , the bullet begins to penetrate the target much more rapidly. The residual velocity from the numerical simulation is 550 m/s.

Position-time for the nose, tail, substrate interface, and back of the aluminum substrate are plotted in Fig. 8. The dotted lines denote the nose and tail of the core. The dashed horizontal lines denote the initial positions of the impact surface, ceramic/metal interface, and the target rear surface. The solid symbols are the experimental data. The position-time results of the numerical simulation are in pretty good agreement with the experimental data.

The projectile length versus time is shown in Fig. 9. The calculated length of the projectile and the core versus time are also plotted in the figure. As already mentioned, the tip of the core does not interact with the target for approximately 8 μs after impact since it is located about 7 mm behind the tip of the lead nose. The length of the

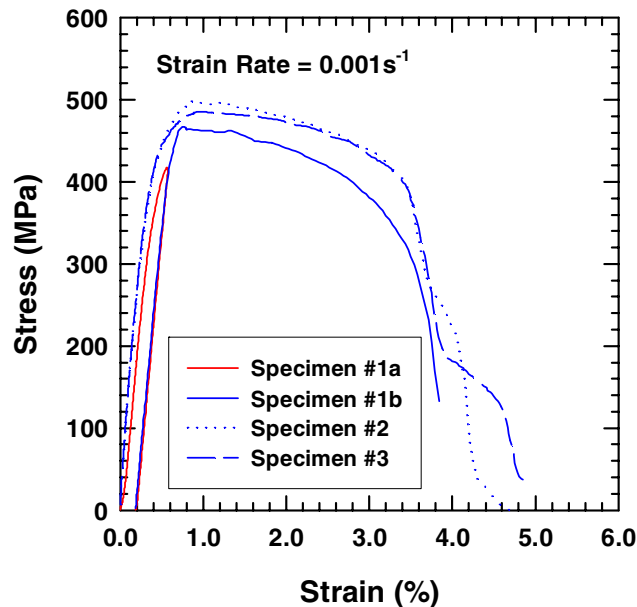


Figure 4 : Stress-strain curve for gilding jacket.

projectile is greater than that of the core after approximately $10 \mu\text{s}$ because the jacket extends slightly beyond the end of the core. The projectile lengths measured from the flash radiographs are plotted as the solid symbols in Fig. 9. Agreement is quite good.

A phenomenon not captured well in the numerical simulations is the separation of the core from the jacket. The tail of the core is visible in Fig. 5(h), and clearly visible in Fig. 5(i) (and Fig. 6). The core, jacket, and eroded projectile material are highlighted by the call outs in Fig. 6. Because the core is significantly stronger than the jacket material, the core undergoes larger deceleration than the jacket; hence, the jacket slides past the core. The length measurements are from the bullet/ceramic interface to the core tail. In the simulation, however, the core and the jacket remain together and do not separate. Dynamics of the jacket, and its interaction with the ceramic, affect the ability of the simulations to reproduce the correct residual velocity, and ultimately, the ballistic limit velocity.

A comparison between the numerical simulation and the flash radiograph at $22.9 \mu\text{s}$ is shown in Fig. 10. One set of dashed lines (the top two) shows that the simulation is scaled appropriately (i.e., the diameter of the bullet is the same in the simulation and the flash radiograph). The other two dashed lines show that the crater radius, and the

radial extent of the debris (probably bullet debris, consisting of lead and jacket material) are quite accurately reproduced in the simulation.

The simulation results are again compared to an X-ray shadowgraph, but now at $30.3 \mu\text{s}$, in Fig. 11. The top two dotted lines run along the edges of the core (instead of the jacket, as in the previous figure). The simulation reasonably reproduces the edge of the debris. However, the material at the penetration front is not as flat in the simulation as in the experiment, which results in two discrepancies: (1) the penetration crater is not as wide, and (2) penetration is too deep in the simulation. The experiments indicate that the penetration front stays quite broad (at least with debris), and this is not captured in the simulation. Because the penetration is not sufficiently broad, the projectile has penetrated deeper in the simulation. The difficulty could be the ceramic model (the comminuted ceramic is not “strong” enough), or perhaps the constitutive model for the core needs to be improved. It is difficult to separate these two issues with one set of data.

By approximately $25 \mu\text{s}$, the projectile is penetrating in a rigid-body or quasi-rigid-body mode, i.e., the nose and tail of the projectile are approximately the same velocity, Fig. 7. As already pointed out, the jacket does not slide over the core in the simulation, as observed in the

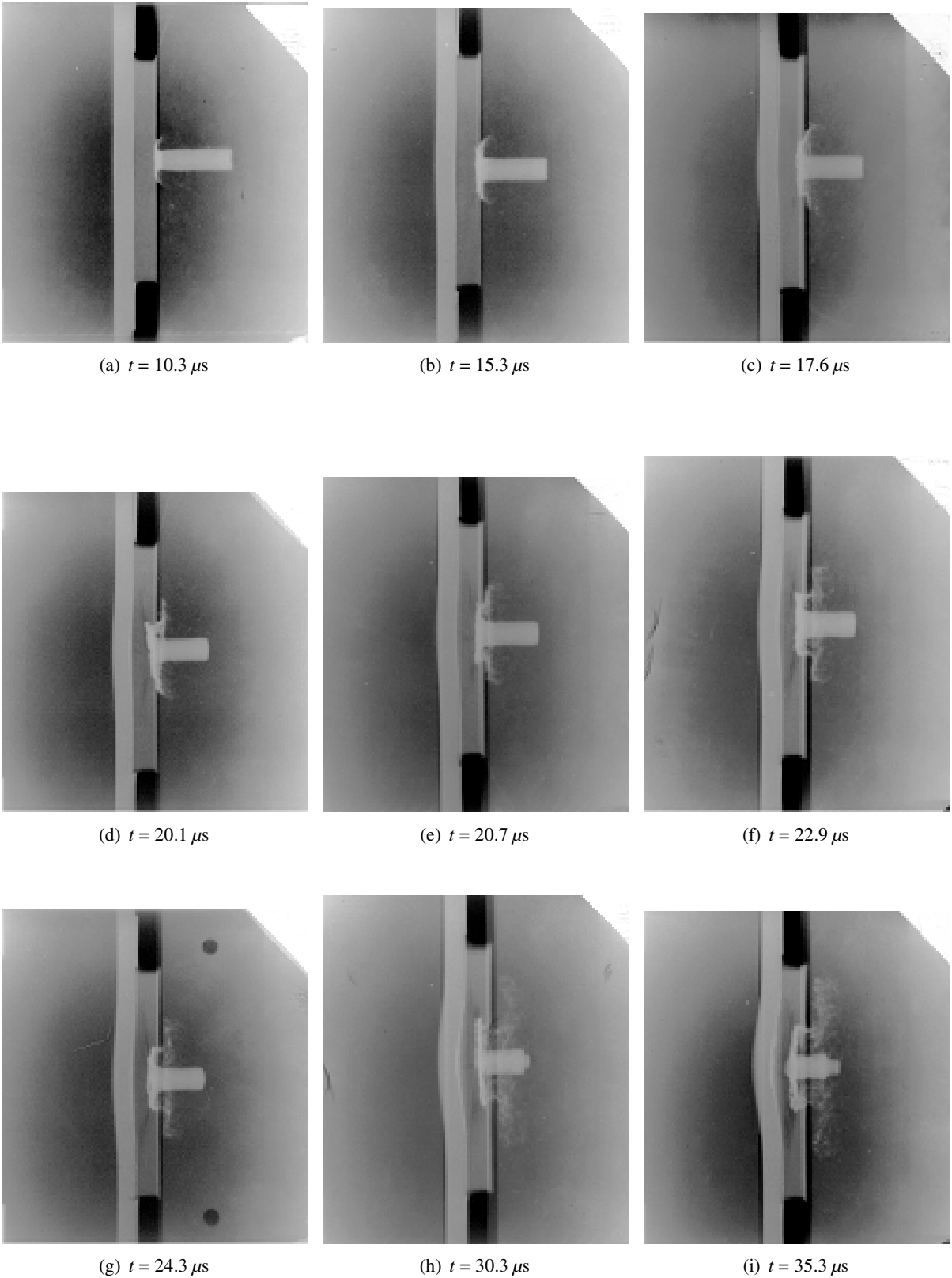


Figure 5 : Flash radiographs from experiments.

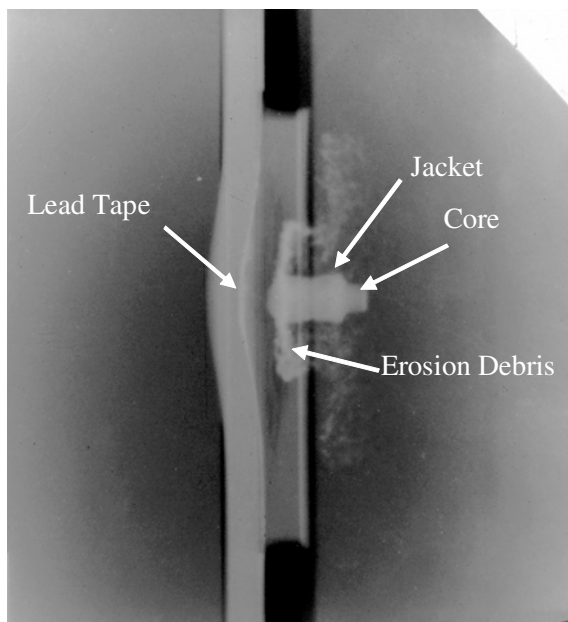


Figure 6 : Enlarged view of radiograph at 35.3 μ s.

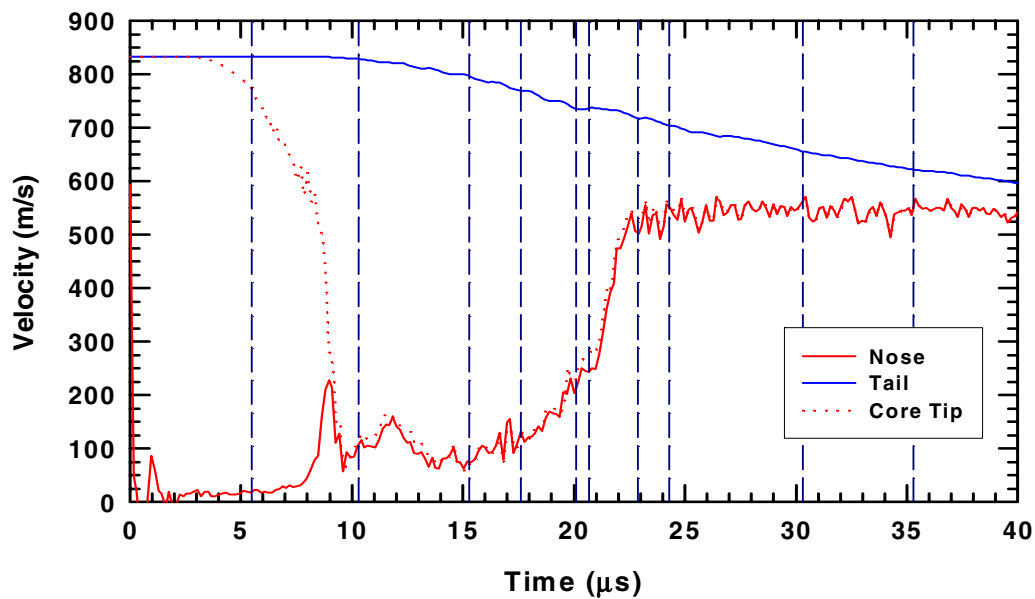


Figure 7 : Nose, core, and tail velocities for APM2 projectile impacting B₄C/6061-T6 target.

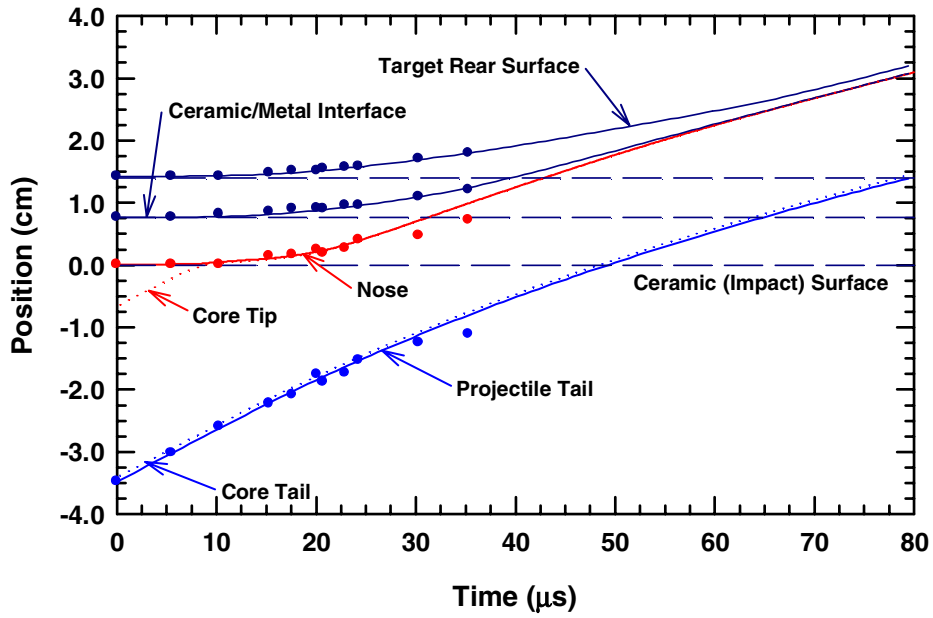


Figure 8 : Position-time for APM2 projectile impacting B₄C/6061-T6 target

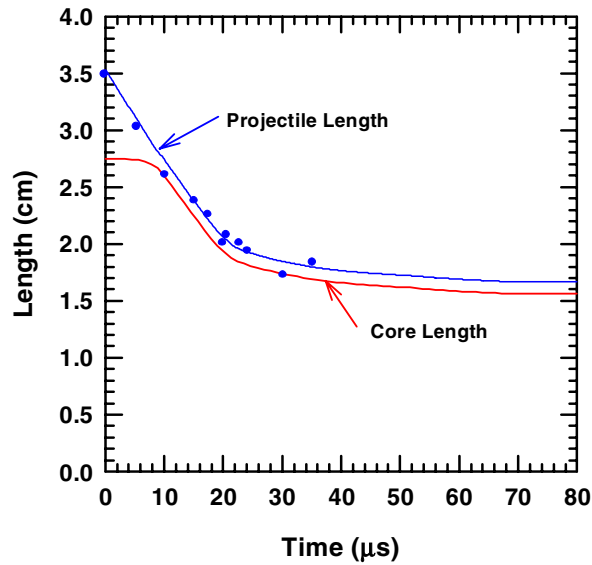


Figure 9 : Projectile and core lengths vs. time.

Table 2 : Experimental Data from Flash Radiography Experiments

Impact Velocity (m/s)	Time (μs)	Nose Position (cm)	Tail Position (cm)	Interface Position (cm)	Back Surface Position (cm)
837	0.00	0.00	-3.48	0.762	1.422
840	5.50	0.00	-3.02	0.762	1.422
844	10.30	0.00	-2.60	0.812	1.422
825	15.30	0.14	-2.23	0.852	1.472
842	17.60	0.16	-2.09	0.902	1.512
851	20.10	0.24	-1.76	0.907	1.512
819	20.70	0.19	-1.88	0.902	1.542
827	22.90	0.26	-1.74	0.952	1.562
833	24.30	0.40	-1.53	0.952	1.582
834	30.30	0.47	-1.25	1.092	1.702
821	35.30	0.72	-1.11	1.202	1.792

experiment. This has an effect at later times since in the experiment the jacket and core become somewhat decoupled. In the simulation, they are very much coupled—the net result is that the effective bullet mass in the simulation, after approximately 25-30 μ s, is probably too large. Simulations where the rearward portion of the jacket was removed (to simulate decoupling of the core and jacket) show that that the early-time penetration behavior is still captured, but residual velocities after perforation are in much better agreement with experiment (near a ballistic limit velocity).

4 Conclusions

A set of ballistic experiments was conducted for the 7.62-mm APM2 bullet against B₄C/Al targets. Flash radiography was used to provide time-resolved penetration histories. A numerical computation, using an engineering computational ceramics model, simulated the experiments, and the computational results were compared to the experimental data. The simulation reproduced the phenomenon of dwell (no-to little penetration for the first \sim 18 μ s), and, for the most part, showed very good agreement with the experimental data. The simulation results agreed very well with the projectile lengths measured from the flash radiographs. The positions of the projectile nose and tail, the ceramic-aluminum interface, and the rear surface of the aluminum were also in very good agreement with the experimental data. Further, crater width and debris diameter from the simulation were in

good agreement with results measured from the flash radiographs.

Several discrepancies between the simulated results and the flash radiographs are apparent, however, at times greater than approximately 25 to 30 μ s. Some of these discrepancies may be interrelated. In the experiments, the core is decelerated faster than the jacket, and the jacket slides down over the core. This observation is not reproduced in the simulations. Also, at 30 μ s and 35 μ s, the simulations overpredict penetration depth, underpredict crater width, and the bullet nose is more conical shaped in the simulation than in the experiments. The fact that the bullet core is “too pointed” could be caused by some errors in the constitutive model for the core (for example, a constant failure strain instead of a pressure-dependent failure strain).

Relative to the computational ceramics model, the constant f_1 —the parameter that controls the time it takes for a computational cell to damage, i.e., go from intact strength to comminuted ceramic—must be specified. Damage initiation is controlled by a tensile stress, subject to the condition that a cell is at a free surface, a material interface, or that a neighboring computational cell is completely damaged. The last of these conditions implies that, in practice, it is the comminution time of the ceramic that controls damage propagation. The mechanics of this comminution are not explicitly modeled; instead, all the mechanics—which is currently not understood—is “lumped” into the adjustable param-

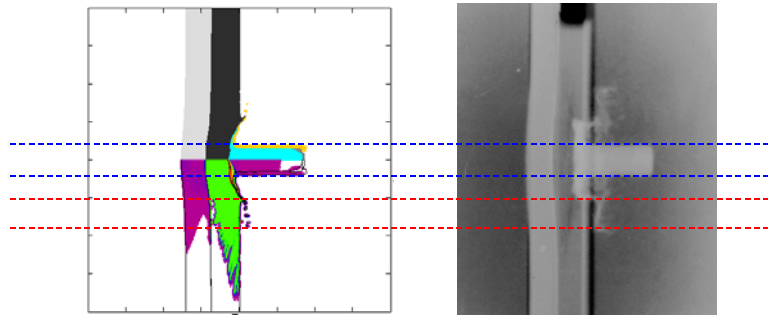


Figure 10 : Comparison of simulation result to X-ray shadowgraph at 22.9 μs .

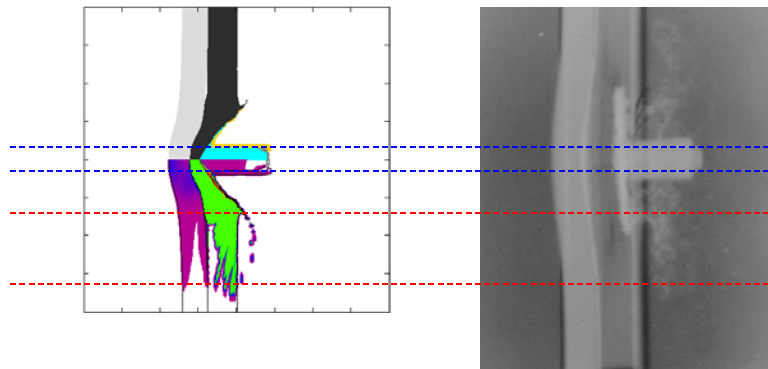


Figure 11 : Comparison of simulation result to X-ray shadowgraph at 30.3 μs .

eter f_1 . Nevertheless, it has been demonstrated that the computational ceramics model can reasonably reproduce time-resolved penetration data into a thin-tiled ceramic target. The model has been applied to a number of engineering problems and has been found to be extremely useful and reasonably accurate for engineering design calculations.

Acknowledgement: The authors gratefully acknowledge the support and encouragement of Ms. Janet Ward from the US Army Chemical and Biological Command and Dr. Steve Wax from DARPA. The authors also wish to thank Mr. Dick Sharron for computational support. This work was funded under contract DAAD16-00-C-9260.

References

- Anderson, Jr. C. E.** (1999): unpublished data.
- Anderson, Jr., C. E.; Walker, J. D.** (2000): Ceramic dwell and defeat of the 0.30-Cal AP projectile, *Proc. 15th U.S. Army Symp. on Solid Mech.*, (Eds: K. Iyer and S-C Chou), pp. 17-28, Battelle Press, Columbus OH.
- Anderson, Jr. C. E.; Gooch, W. A.** (2001): Numerical Simulations of dynamic X-ray imaging experiments of 7.62-mm APM2 projectiles penetrating B₄C, *Proc. 19th Int. Symp. on Ballistics*, vol. 3, pp. 1423-1429, Interlaken, Switzerland, May 7-11.
- Anderson, Jr. C. E.** (2003), From fire to ballistics: A historical retrospective, *Int. J. Impact Engng.*, vol. 29, pp. 13-67.
- Atluri, S. N.; Han, Z. D.; Rajendran, A. M.** (2004): A new implementation of the meshless finite volume method through the MLPG mixed approach, *CMES: Computer Modeling in Engineering & Sciences*, vol. 6, no. 6, pp. 491-514.
- Bardenhagen, S. G.; Kober, E. M** (2004): The generalized interpolation material point method, *CMES: Computer Modeling in Engineering & Sciences*, vol. 5, no. 6, pp. 477-496.
- Gooch, W. A.; Burkins, M. S.; Kingman, P.; Hauver, G.; Netherwood, P.; Benck, R.** (1999): Dynamic X-ray imaging of 7.62-mm APM2 projectiles penetrating boron carbide, *Proc. 18th Int. Symp. on Ballistics*, vol. 2, pp. 901-908, Technomic Publishing Company, Inc., Lancaster, PA.
- Gooch, W. A.; Burkins, M. S.; Hauver, G.; Nether-**

- wood, P.; and Benck, R.** (2000): Dynamic X-rays imaging of the penetration of boron carbide, *J. Phys. IV France*, vol. 10, Pr9-593-588.
- Holmquist, T. J.; Johnson, G. R.** (2002): A detailed computational analysis of interface defeat, dwell and penetration for a variety of ceramic targets, *Proc. 20th Int. Symp. on Ballistics*, vol. 2, pp. 746-753, DEStech Publications, Lancaster, PA.
- Johnson, G. R.; Cook, W. H.** (1983): A constitutive model and data for metals subjected to large strains, high strain rates and high temperatures, *Proc. 7th Int. Symp. on Ballistics*, pp. 541-548, The Hague, The Netherlands, 19-23 April.
- Johnson, G. R.** (1999): private communication.
- Johnson, G. R.; Holmquist, T. J.** (1999): Response of boron carbide subjected to large strains, high strain rates, and high pressures, *J. Appl. Phys.*, vol. 85, no. 12: pp. 8060-8073.
- Johnson, G. R.; Beissel, S. R.; Stryk, R. A.** (2000): A generalized particle algorithm for high velocity impact calculations, *Comp. Mech.*, **25**, 245-256.
- Johnson, G. R.; Beissel, S. R.; Holmquist, T. J.** (2002): Improved computational modeling of ballistic problems using meshless particles and finite elements, *Proc. 20th Int. Symp. on Ballistics*, vol. 2, pp. 850-858, DEStech Publications, Lancaster, PA.
- Johnson, G. R.; Stryk, R. A.; Beissel, S. R.; Holmquist, T. J.** (2002): An algorithm to automatically convert distorted finite elements into meshless particles during dynamic deformation, *Int. J. Impact Engng.*, vol. 27, no. 10, pp. 997-1013.
- McGlaun, J. M.; Thompson, S. L.; Elrick, M. G.; CTH** (1990): A three-dimensional shock wave physics code, *Int. J. Impact Engng.*, **10**(1-4), pp. 351-360.
- Palika, R.** (1999): Cercom, Inc., private communication.
- Predebon, W. W.; Anderson, Jr., C. E.; Walker, J. D.** (1991): Inclusion of evolutionary damage measures in Eulerian wavecodes, *Comp. Mech.*, vol. 7, no. 4, pp. 221-236.
- Shockey, D. A.; Marchand, A. H.; Skaggs, S. R.; Cort, G. E.; Burkett, M. W.; Parker, R.** (1990): Failure phenomenology of confined ceramic targets and impacting rods, *Int. J. Impact Engng.*, vol. 9, no. 3, pp. 263-275.
- Stecher, F. P.; Johnson, G. R.** (1984): Lagrangian computations for projectile penetration into thick plates, *Computers in Engineering 1984* – vol 2, ASME, pp. 292-299.
- Steinberg, D. J.** (1996): Equation of state and strength properties of selected materials, Change 1, UCRL-MA-106439, Lawrence Livermore National Laboratory, Livermore, CA, Feb.
- Walker, J. D.; Anderson, Jr., C. E.; Cox, P. A.** (1995), Computational modeling of thin AD-85 ceramic tiles backed by thin aluminum substrates, *Proc. 15th Int. Symp. on Ballistics*, vol. 1, pp. 395-402, Jerusalem, Israel, May 21-24.
- Walker, J. D.; Anderson, Jr. C. E.; Cox, P. A.** (1995): Computational modeling of thin ceramic tiles backed by thin substrates, AMD-Vol. 205, *Impact, Waves, and Fracture* (Eds: R. C. Batra, A. K. Mal, and G. P. MacSithigh), pp. 375-390, ASME, NY.
- Wilkins, M. L.** (1968): Third Progress Report of Light Armor Program, UCRL-50460, Lawrence Livermore Laboratory, Livermore, CA.
- Wilkins, M. L.; Landingham, R. L.; Honodel, C. A.** (1970): Fifth Progress Report of Light Armor Program, UCRL-50980, Lawrence Livermore Laboratory, Livermore, CA.
- Wilkins, M. L.** (1978): Mechanics of penetration and perforation, *Int. J. Engng. Sci.*, vol. 16, no. 11, pp. 793-807.
- Wilkins, M. L.** (1981): Calculation of elastic-plastic flow, UCRL-7322, Rev. 2, Lawrence Livermore National Laboratory, Livermore, CA.

Appendix A: Wilkins Ceramic Model

The ceramics model developed by Wilkins [Wilkins (1968), Wilkins (1978)] was originally implemented into the Lagrangian finite-difference wavecode HEMP [Wilkins (1981)]. We placed the model into the Eulerian finite-difference wave propagation code CTH [McGlaun, Thompson, and Elrick (1990)]. The essential features of this model, as modified to make the model consistent with an Eulerian implementation, are as follows.

1. Fracture begins on surfaces. In the Eulerian framework, we choose to define a surface as being comprised of those cells that are a given number of cells (usually one) away from a mixed cell. A cell is mixed if it contains two or more materials or contains void. Thus, those cells that are in close prox-

imity to the actual surfaces in the calculation are viewed as possible initiation sites for fracture. The axis of symmetry is not considered a surface.

2. The criterion for fracture is that a principal stress in the plane of motion is greater than σ_f , where stresses are positive in tension. $\sigma_f \geq 0$ is a material constant that depends upon the ceramic.
3. There is a time delay for complete fracture of a cell. This time delay is related to the time for a crack to propagate across a computational cell. The speed of crack propagation V_c is assumed to be a fraction of the elastic shear wave speed:

$$V_c = f_1 \sqrt{G/\rho} \quad (\text{A1})$$

where G is the shear modulus, ρ is the ceramic material density, and $0 < f_1 \leq 1.0$. A typical value for f_1 used by Wilkins is 0.5. This aspect of the model is necessary to keep the fracture algorithm from propagating failure through the computational mesh at unrealistically high speeds. In particular, it precludes adjacent cells from fracturing each computational cycle.

4. A cell that has fractured becomes the source of fracture for a nearby cell.
5. The extent of fracture in a computational cell is tracked with the internal state variable ϕ_f , where ϕ_f is the fraction of the material in the cell that has fractured. Thus, $0 \leq \phi_f \leq 1.0$; $\phi_f = 0$ implies no fracture has occurred with a cell, and $\phi_f = 1.0$ implies the material in a cell has completely fractured.
6. The fracture of a cell is accomplished by setting the strength of the material to zero. Thus, the strength of the fractured material within a cell is given by:

$$Y = (1 - \phi_f) Y_o \quad (\text{A2})$$

where Y_o is the intact strength that depends upon the specific ceramic. A cell in which the material has completely fractured thus has no shear strength ($Y = 0$). The completely fractured material acts fluid-like, with a bulk response defined by the equation of state of the material.

We emphasize that a cell can begin to fracture if its maximal principal stress is greater than σ_f and a contiguous

neighbor cell either has completely fractured ($\phi_f = 1$) or is at a surface. This criterion allows the crack to follow its own path, based on the stress state of the material. The crack speed is controlled by the time it takes a cell to completely fracture. Once a cell begins to fracture, it continues to fracture at the same rate regardless of the stress state:

$$\frac{d\phi_f}{dt} = \frac{V_c}{X} \quad (\text{A3})$$

where X is a characteristic length of a computational cell, and V_c is given by Eq. (A1). In two dimensions, $X = [(\Delta x)(\Delta y)]^{1/2}$ where Δx is the length of the cell in the x direction, and Δy is the length of the cell in the y direction. This is used for both Cartesian and cylindrical coordinates.

Since a cell's neighbor must completely fracture before the cell can begin to fracture, the maximum propagation speed for the crack is V_c . Once fracture begins it goes to completion.

Appendix B: Modified Wilkins Ceramic Model

We found that the Wilkins ceramic model, as published, needed to be modified to match experimental data. In particular, it was determined that the failed ceramic material had to have strength. Assuming that portion of the failed ceramic material that interacts with the projectile is highly comminuted, then the flow stress is given by a Drucker-Prager model:

$$Y_f = \begin{cases} 0 & P < 0 \\ bP & 0 \leq P < Y_{cap}/b \\ Y_{cap} & P \geq Y_{cap}/b \end{cases} \quad (\text{B1})$$

where P is the hydrostatic pressure (mean stress), b is a material dependent parameter, and Y_{cap} represents the maximum stress that can be supported by the failed material. The value Y_{cap}/b is the pressure at which the stress cap is reached. As the ceramic fails, the flow stress is a function of the volume fraction of intact and failed material:

$$Y = (1 - \phi_f) Y_o + \phi_f Y_f \quad (\text{B2})$$

The original model considered fracture only in the plane of motion. Our implementation also permits fracture based on hoop stresses ($\sigma_{\theta\theta}$). This is a physically reasonable criterion for brittle fracture. One other option

was also incorporated into the modified model. Once a computational cell has fractured, the cell can fail immediately (i.e., go from intact strength to “failed” strength in one cycle), or the strength can be relaxed over the time for the fracture to propagate across the zone. This latter option was used in all the calculations in this paper.

The constants required for the model are: the intact strength Y_o , the tensile fracture stress σ_f , the slope of the Drucker-Prager curve b , the cap Y_{cap} , the shear modulus G , and the density ρ . (Since the bulk modulus κ is specified for the equation of state, Poisson’s ratio can be specified in lieu of G .) The constant f_1 must be specified, and whether failure is permitted in the hoop direction or only in the plane of motion must also be specified.

Appendix C: Sensitivity of Results to Model Parameters

Model parameters were determined from values provided in the literature, as described in the main text, except for the value of f_1 . The parameter f_1 was found by requiring that the simulations reproduce the eroded length of the APM2 core as well as the residual velocity for B₄C/Al targets that were overmatched (i.e., were perforated). The core is eroded solely by the ceramic; thus, the core length was a direct diagnostic for the ceramic model. Literally, many tens of simulations were conducted, because at the time of the original work, the slope and cap of the Drucker-Prager model for the failed ceramic also had to be determined. Later, Johnson and Holmquist (1999) found independent data that confirmed the Drucker-Prager values that had been determined by requiring simulations to match experimental data. Nevertheless, f_1 is not independent of some of the other model constants. For example, if the intact strength was changed to a smaller value (say from 12 GPa to 6 GPa), then f_1 might have to be changed since the influence of the strength of the intact material dominates—along with f_1 —the time of dwell. Likewise, the value used for the failure strain for the core could have an influence on the value for f_1 because of the nonlinear coupling between the ceramic model and erosion of the core. These comments are provided for additional insights into the model parameters and their interdependence; but, these caveats do not preclude the usefulness of the model, as we have used it extensively and successfully for analysis and design applications.